Angewandte Chemie
Eine Zeitschrift der Gesellschaft Deutscher Chemiker

Supporting Information

Magnetization Dynamics on Isotope-Isomorphic Holmium Single-Molecule Magnets

Yang Liu[+], Le Tuan Anh Ho[+], Guo-Zhang Huang, Yan-Cong Chen, Liviu Ungur, Jun-Liang Liu,* and Ming-Liang Tong*

anie_202112764_sm_miscellaneous_information.pdf
anie_202112764_sm_cif.zip

Supporting Information

Contents

1. Experimental section

All reactions and manipulations described below were performed under nitrogen conditions by using Schlenk techniques. Metal salts and other reagents were commercially available and used as received without further purification. The C, H, and N elemental analyses were carried out with an Elementar Vario-EL CHNS elemental analyzer. Infrared spectra (4000−500 cm^{-1}) were recorded by using Attenuated Total Reflectance (ATR) technique at room temperature on PerkinElmer Frontier FT-IR spectrometer and KBr pellet on NICOLET 6700. Thermogravimetric (TG) analysis was carried out on a TG-209 F3 Tarsus thermogravimetric analyzer. All magnetic measurements were performed on polycrystalline samples sealed in polyethylene bag with small amount of mother liquor. Ac magnetic measurements were performed at frequencies from 0.1 to 999 Hz. Magnetic susceptibility measurements were performed with a Quantum Design MPMS-3 magnetometer. Data were corrected for the diamagnetic contribution from empirical data. To avoid the protium-deuterium exchange, the samples were well sealed with a small amount of mother liquor. And the weights of the samples were later obtained after the measurements had finished. Single-crystal diffraction data were collected on a Bruker D8 QUEST diffractometer with Mo-K_α radiation (λ = 0.71073 Å) for complex **1** and **2** at 120 K. The data collection and reduction were carried out using the Bruker APEX3 program for **1** and **2**. The structures were solved by SHELXT methods with Olex2 program,[1,2] and all non-hydrogen atoms were refined anisotropically by least-squares technique on weighted F^2 using the SHELXL.[3] Anisotropic thermal parameters were assigned to all non-hydrogen atoms. The hydrogen atoms attached to C and N atoms were placed in idealized positions. X-ray powder diffraction intensities for polycrystalline samples were measured on SmartLab X-ray Diffractometer (Cu-K_α, λ = 1.54056 Å) at room temperature.

Synthesis of $[Ho(CyPh_2PO)_2(H_2O)_5]I_3 \cdot 2(CyPh_2PO) \cdot 2EtOH$ (1) The synthetic reaction is similar to that reported previously.[4] The ultra-dry HoI_3 (0.2 mmol, 0.109 g) and $CyPh_2PO$ (0.8 mmol, 0.227 g) were mixed in H_2O/EtOH [1/9 (v/v), 5 mL] solution. And then the mixture was vapored under nitrogen flow. Colorless crystals suitable for X-ray analysis began to grow after 2 days (yield *ca.* 50 %). Anal. calcd (%) for $C_{76}H_{106}HoI_3O_{11}P_4$: C 48.94, H 5.73, N 0.00. Found (%) C 48.72, H 5.80, N 0.00.

Synthesis of $[Ho(CyPh_2PO)_2(D_2O)_5]I_3 \cdot 2(CyPh_2PO) \cdot 2EtOD$ (2) The ultra-dry HoI_3 (0.2 mmol, 0.109 g) and $CyPh_2PO$ (0.8 mmol, 0.227 g) were mixed in D_2O/EtOD [1/9 (v/v), 5 mL] solution. And then the mixture was vapored under nitrogen flow. Colorless crystals suitable for X-ray analysis began to grow after 2 days (yield *ca.* 50 %). Anal. calcd (%) for $C_{76}H_{94}D_{12}HoI_3O_{11}P_4$: C 48.63, 5.69, N 0.00. As the EA result is based on taking the mass of all hydrogen isotopes as H, for better compare with the given experimental result, the calculated H content is herein calculated as (94+12)*1.00794/1877.19*100%=5.69%. Found (%) C 48.53, H 5.79, N 0.24.

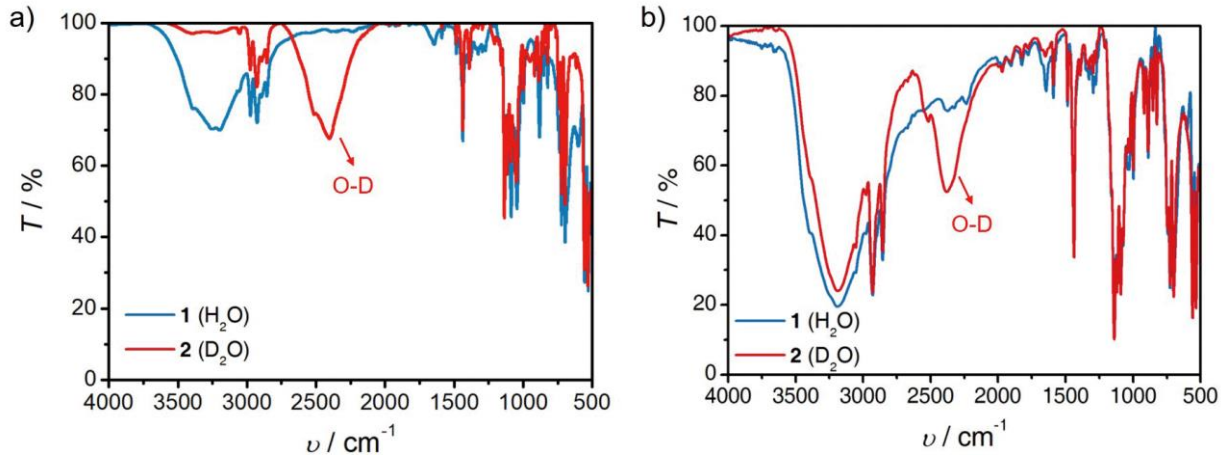

Figure S1. Infrared spectra of **1** (blue) and **2** (red) using attenuated total reflection and the sample were further protected by a small amount of mother liquor (a), and using KBr pellet for the dry sample (b). The infrared spectrum confirms that complex **2** does show O−D stretching vibration around 2405 cm^{-1} in both (a) and (b), while complexes **1** shows O−H stretching vibration around 3200 cm^{-1}. This result testifies to the fact that the deuterium of water and ethanol can prevent it from exchanging into protium under a small amount of mother liquor.

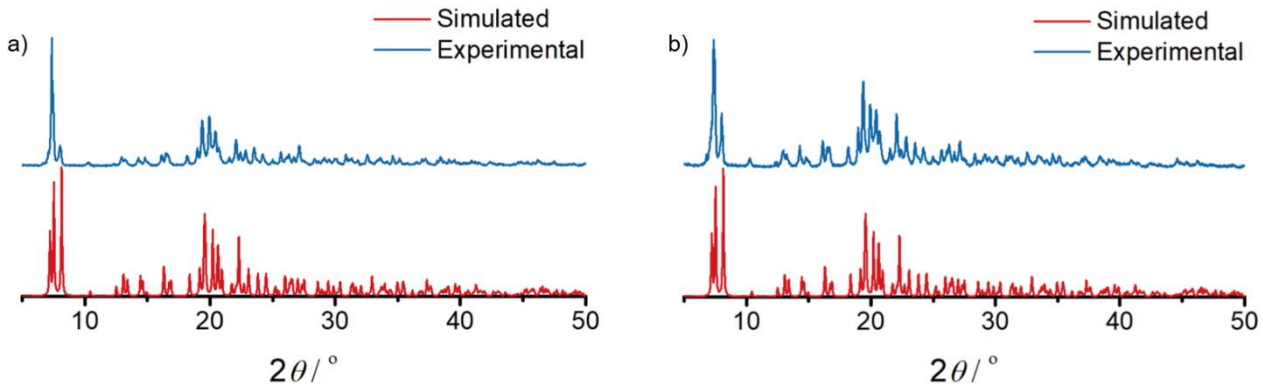

Figure S2. Experimental and calculated X-ray powder diffraction patterns for **1** (a) and **2** (b).

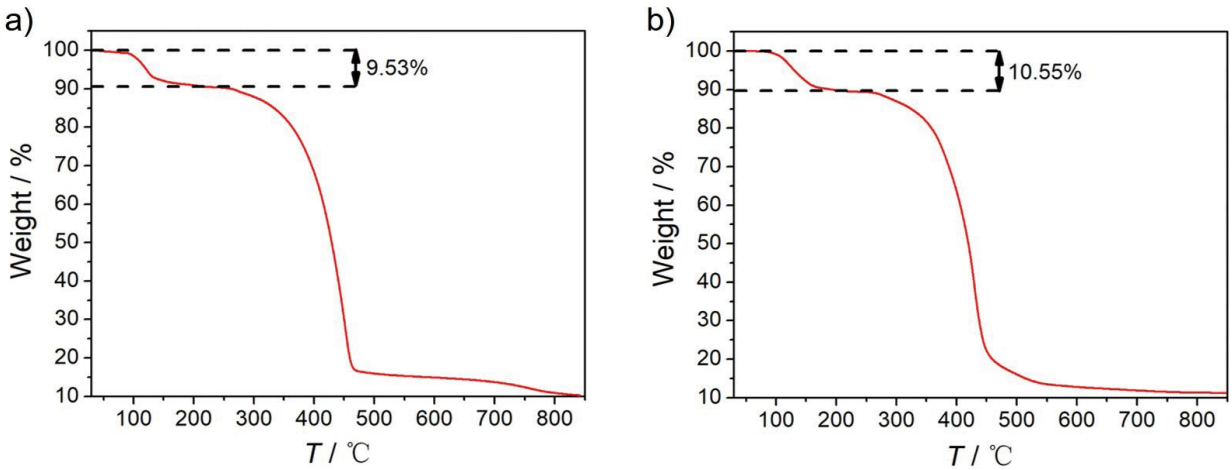

Figure S3. Thermogravimetric analysis for **1** (a) and **2** (b) under N_2 atmosphere.

2. X-ray single-crystal diffraction

Table S1. Crystal data and structure refinement for **1** and **2**.

Complexes	**1**	**2**
Formula	$C_{76}H_{106}HoI_3O_{11}P_4$	$C_{76}H_{94}D_{12}HoI_3O_{11}P_4$
M_r / g mol^{-1}	1865.11	1877.19
T / K	120	120
Crystal System	orthorhombic	orthorhombic
Space Group	$C222_1$	$C222_1$
a / Å	14.0997(7)	14.1103(6)
b / Å	24.5137(11)	24.5165(9)
c / Å	23.5115(10)	23.5263(8)
α / °	90	90
β / °	90	90
γ / °	90	90
V / Å^3	8126.4(6)	8138.6(5)
Z	4	4
ρ_{calcd} / g cm^{-3}	1.524	1.532
F(000)	3744	3744
Reflections collected	35790	35195
Independent reflections	7966	7995
GOF on F^2	1.083	1.047
R_1, wR_2 [$I \geq 2\sigma(I)$][a]	0.0326, 0.0706	0.0382, 0.0769
R_1, wR_2 (all data)[b]	0.0349, 0.0715	0.0485, 0.0798
CCDC number	2110632	2110633

[a]$R_1 = \Sigma||F_o| - |F_c||/\Sigma|F_o|$. [b]$wR_2 = [\Sigma w(F_o^2 - F_c^2)^2/\Sigma w(F_o^2)^2]^{1/2}$

Table S2. Selected bond lengths (Å) and bond angles (°) for **1** and **2**.

Bond	**1**	**2**	**Bond angle**	**1**	**2**
Ho1–O1	2.202(4)	2.196(5)	O1–Ho1–O1A	177.9(2)	177.8(3)
Ho1–O1A	2.202(4)	2.196(5)	O1W–Ho1–O2W	71.65(11)	71.49(13)
Ho1–O1W	2.334(5)	2.333(6)	O2W–Ho1–O3W	72.47(16)	72.60(18)
Ho1–O2W	2.354(4)	2.353(5)	O3W–Ho1–O3WA	72.0(2)	72.1(3)
Ho1–O2WA	2.354(4)	2.353(5)	O3WA–Ho1–O2WA	72.47(16)	72.59(18)
Ho1–O3W	2.342(4)	2.341(5)	O2WA–Ho1–O1W	71.65(11)	71.49(13)
Ho1–O3WA	2.342(4)	2.341(5)			

Symmetry code (A): -1-x, +y, -1/2-z.

Table S3. CShM values calculated by SHAPE 2.1 for **1**, **2**.

Complex	**HP-7** (***D*****$_{7h}$**)	**HPY-7** (***C*****$_{6v}$**)	**PBPY-7** (***D*****$_{5h}$**)	**COC-7** (***C*****$_{3v}$**)	**CTPR-7** (***C*****$_{2v}$**)	**JPBPY-7** (***D*****$_{5h}$**)	**JETPY-7** (***C*****$_{3v}$**)
1	34.691	25.802	*0.143*	7.520	5.668	2.708	24.553
2	34.674	25.813	*0.149*	7.551	5.695	2.676	24.547

HP-7 = Heptagon, HPY-7 = Hexagonal pyramid, PBPY-7 = Pentagonal bipyramid, COC-7 = Capped octahedron, CTPR-7 = Capped trigonal prism, JPBPY-7 = Johnson pentagonal bipyramid J13, JETPY-7 = Johnson elongated triangular pyramid J7.

3. Magnetic characterization

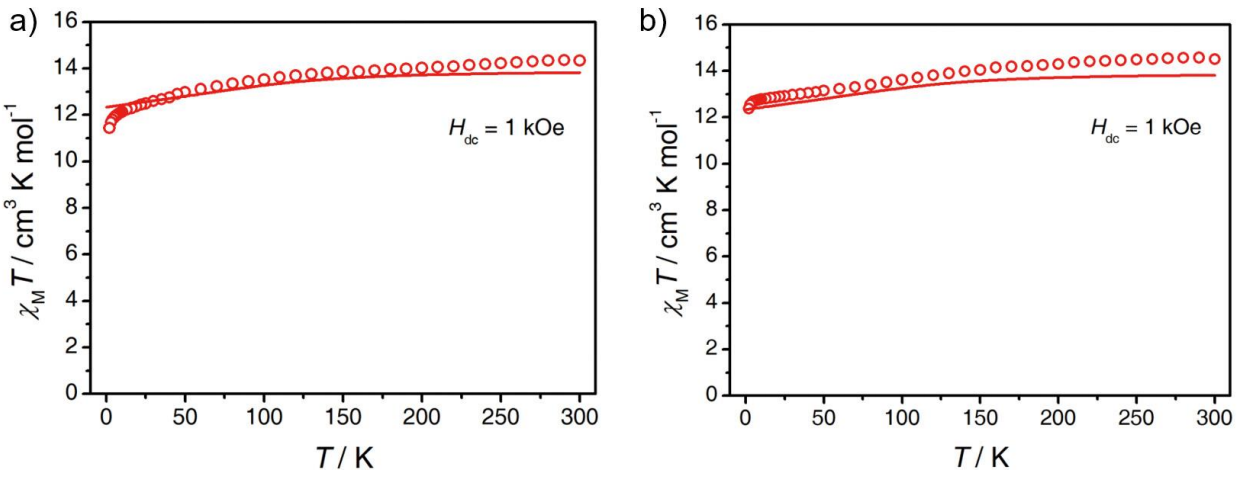

Figure S4. Temperature dependence of the molar magnetic susceptibility $\chi_M T$ products under 1 kOe dc field for **1** (a) and **2** (b). At room temperature, $\chi_M T$ values are respectively 14.33 and 14.50 cm^3 K mol^{-1} for **1** and **2**, which are both slightly larger than that of one isolated Ho(III) (14.07 cm^3 K mol^{-1}). The lines represent the *ab initio* calculated $\chi_M T$ data.

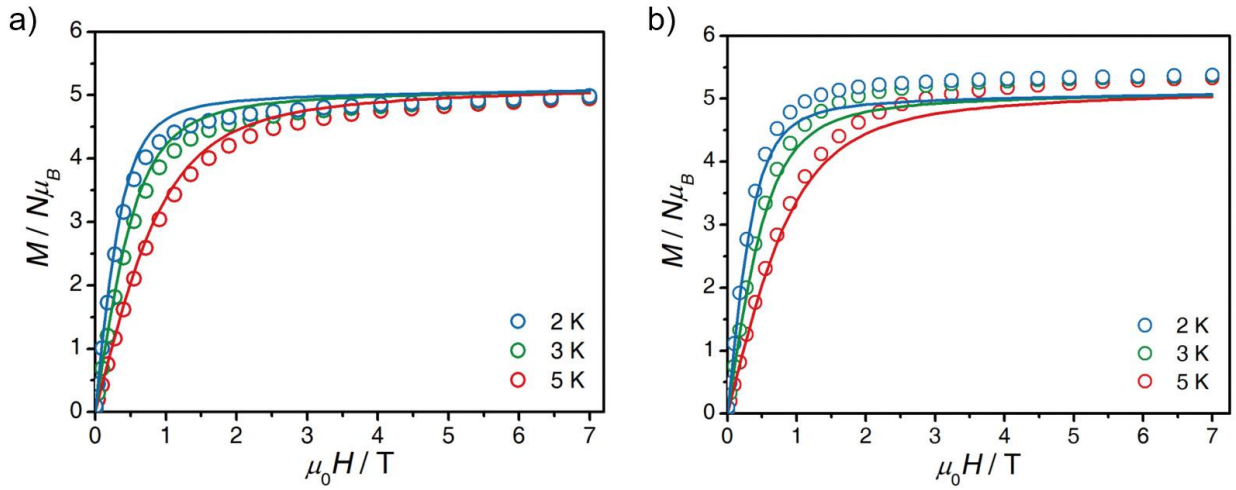

Figure S5. Variable-field magnetization data for **1** (a) and **2** (b). Data were collected from 0−7 T in steady fields. The lines represent the *ab initio* calculated $\chi_M T$ data.

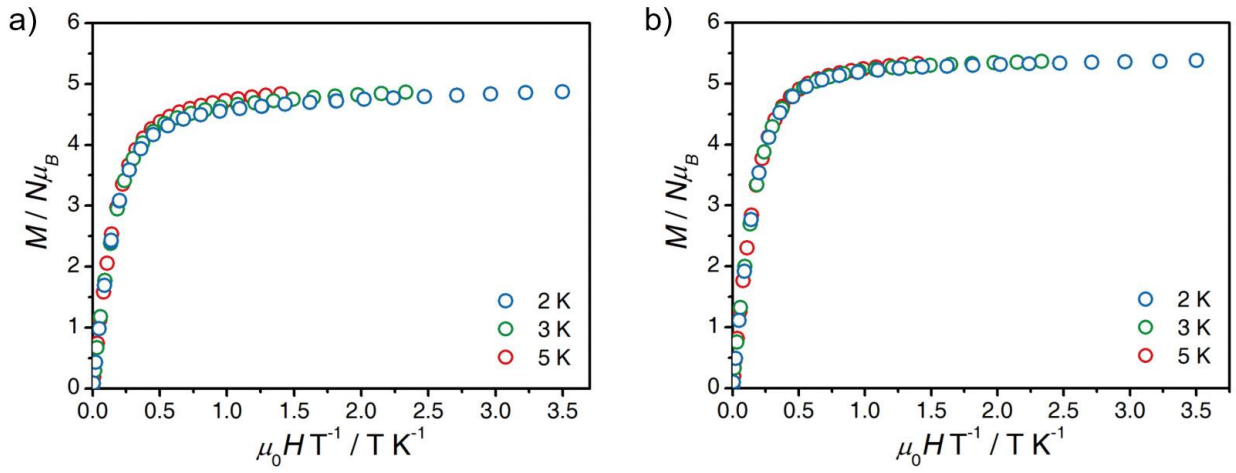

Figure S6. The plot of *M vs*. $\mu_0 H/T$ for compound **1** (a) and **2** (b) at different temperatures.

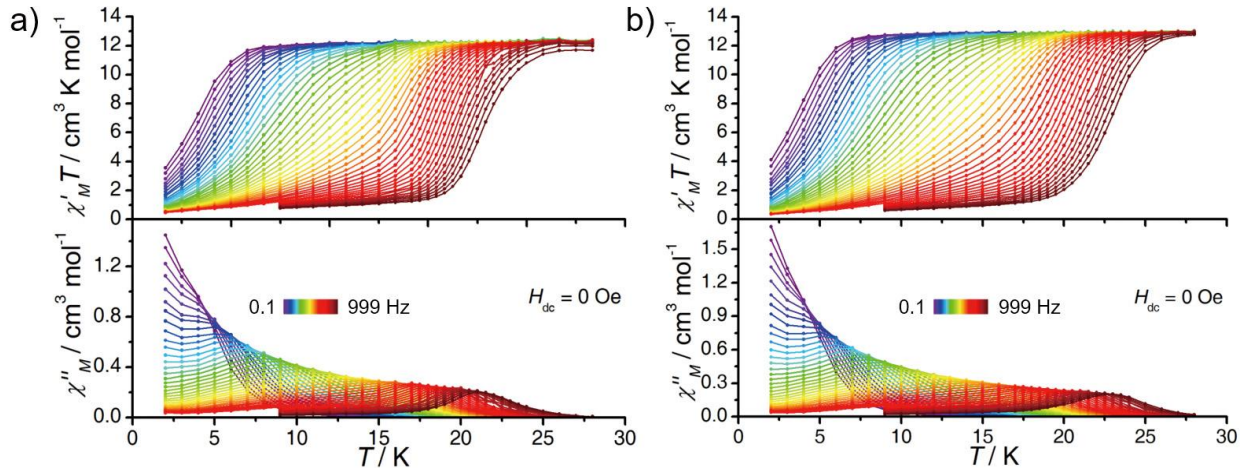

Figure S7. Temperature dependence of the in-phase $\chi_M'T$ product and out-of-phase χ_M'' for **1** (a) and **2** (b) under a zero dc field. The solid lines are guides for the eyes. In a zero dc field, temperature dependence of ac magnetic susceptibilities exhibits the maximum of χ_M'' (999 Hz) located at 21 K (**1**) and 23 K (**2**) respectively.

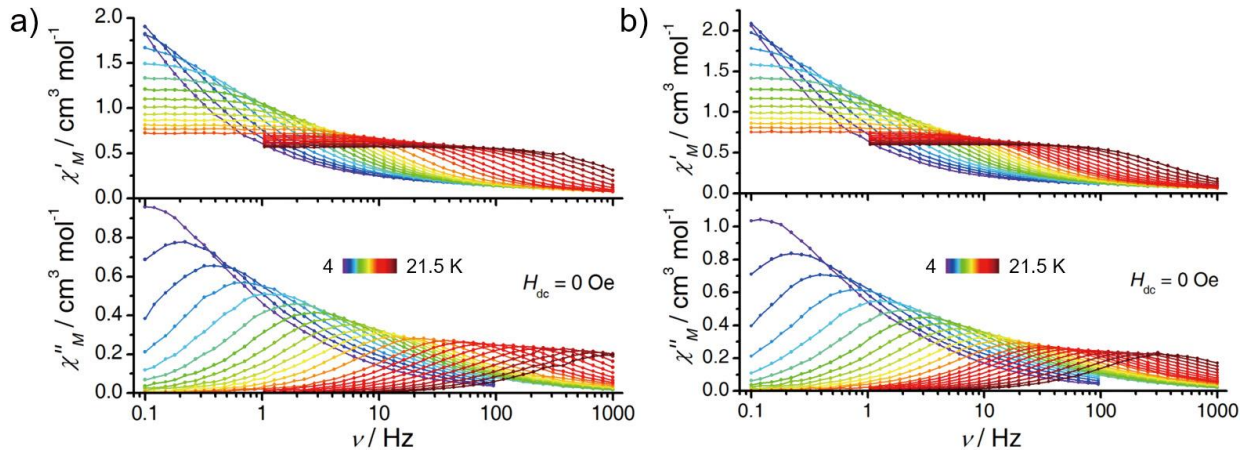

Figure S8. Frequency dependence of ac magnetic susceptibilities at variable temperatures for **1** (a) and **2** (b) under a zero dc field. The solid lines are guides for the eyes.

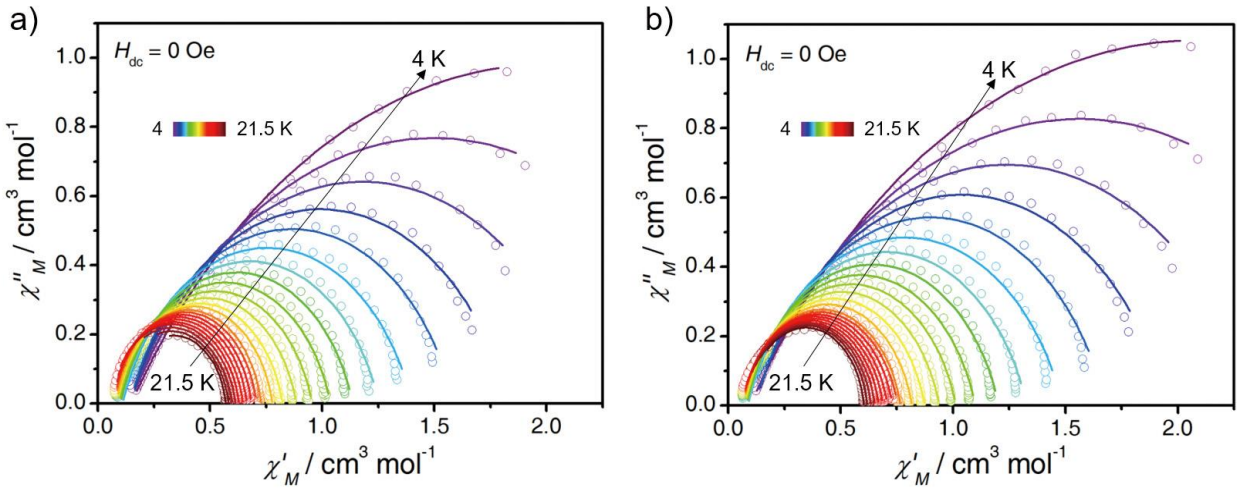

Figure S9. Cole-Cole plots for the ac susceptibilities for **1** (a) under a zero dc field (α = 0.1-0.38), and for **2** (b) under a zero dc field (α = 0.003-0.37). The solid lines are best fit for the generalized Debye model.

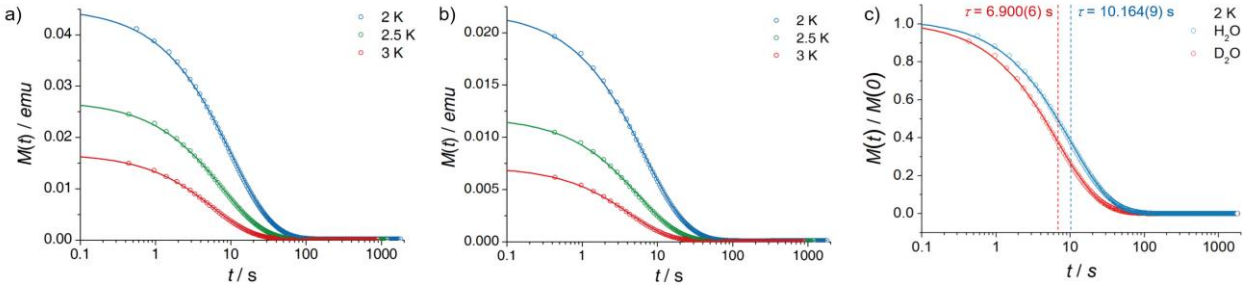

Figure S10. DC magnetization decay of **1** (a) and **2** (b) under zero dc field at 2, 2.5 and 3 K. (c) The DC magnetization data at 2 K were normalized and compared, with the relaxation time of 10.164(9) s and 6.900(6) s for **1** and **2**, respectively. The magnetic field was ramped to 3 T and the temperature was declined to the indicated temperature. After temperature and magnetic moment are steady, the magnetic field was started to reach zero dc field, and kept unchanged for at least 900 ~ 1800 s depending on the measured temperature. During the procedure, the magnetization kept measuring. The solid lines are the best fit to the exponential decay as $M(t) = M_f + (M_i - M_f) \exp[-(t/\tau)^{\beta}]$, where τ is the relaxation time.

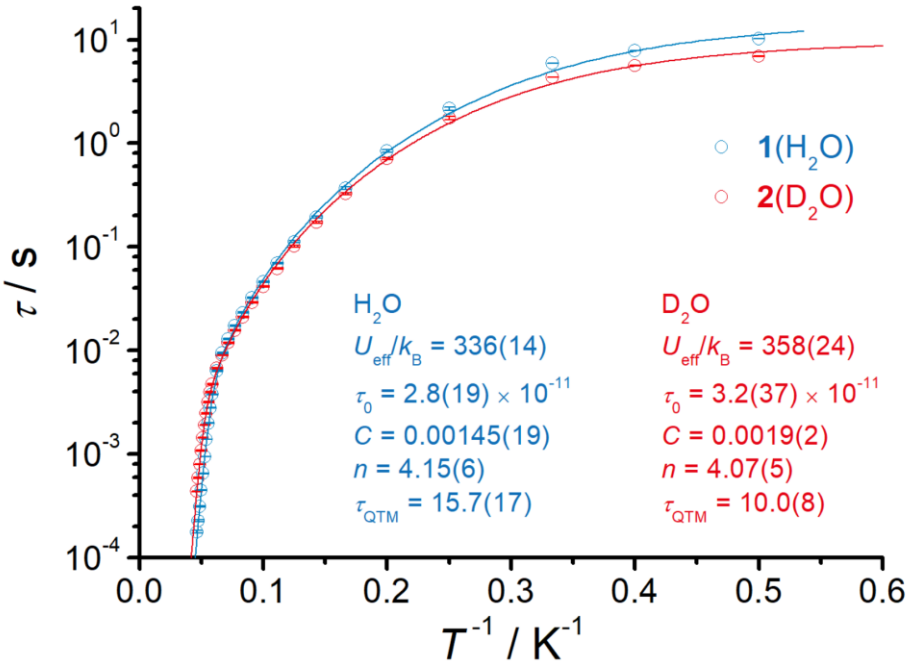

Figure S11. Temperature dependence of the relaxation time τ in a zero dc field for **1** (blue) and **2** (red). The relaxation times can be fitted with the equation, $\tau^{-1} = \tau_0^{-1}\exp(-U_{eff}/k_BT) + CT^n + \tau_{QTM}^{-1}$. At high temperatures, the relaxation times perfectly obey the Arrhenius law with U_{eff}/k_B = 336(14) K and $\tau_0 = 2.8(19)\times10^{-11}$ s for **1**. At low temperatures, the relaxation is generally dictated by the Raman process with C = 0.00145(19) s^{-1} K^{-n}, n = 4.15(6) and finally limited by τ_{QTM} = 15.7(17) s. The deuterated analog, complex **2**, shows similar behavior with U_{eff}/k_B = 358(24) K, $\tau_0 = 3.2(37)\times10^{-11}$ s, n = 4.07(5), C = 0.0019(2) s^{-1} K^{-n} and τ_{QTM} = 10.0(8) s.

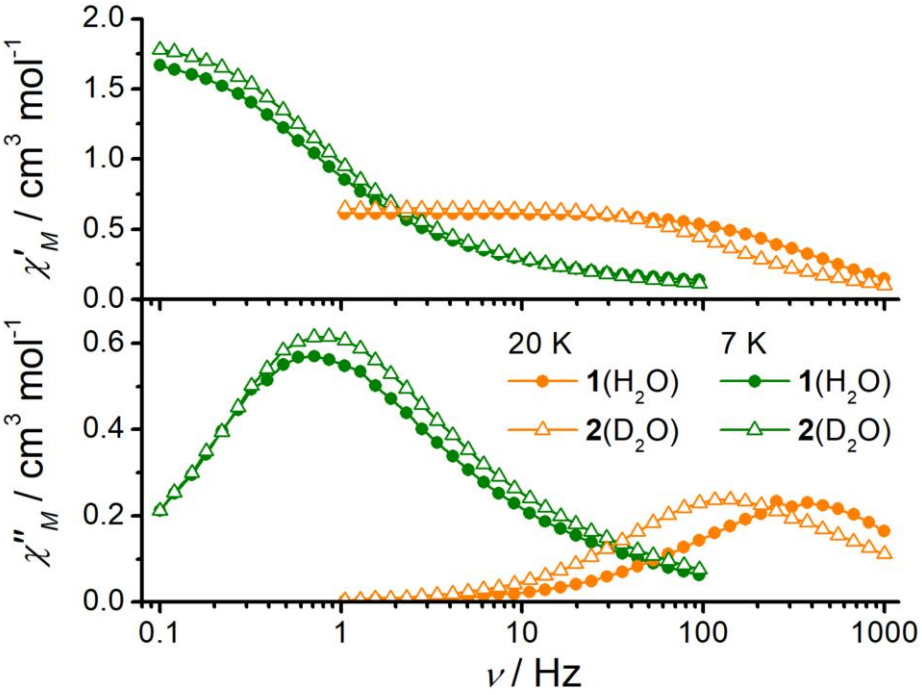

Figure S12. Frequency dependence of ac magnetic susceptibilities for **1** (solid circle) and **2** (empty triangle) under a zero dc field at 7 K (green) and 20 K (orange). The solid lines are guides for the eyes.

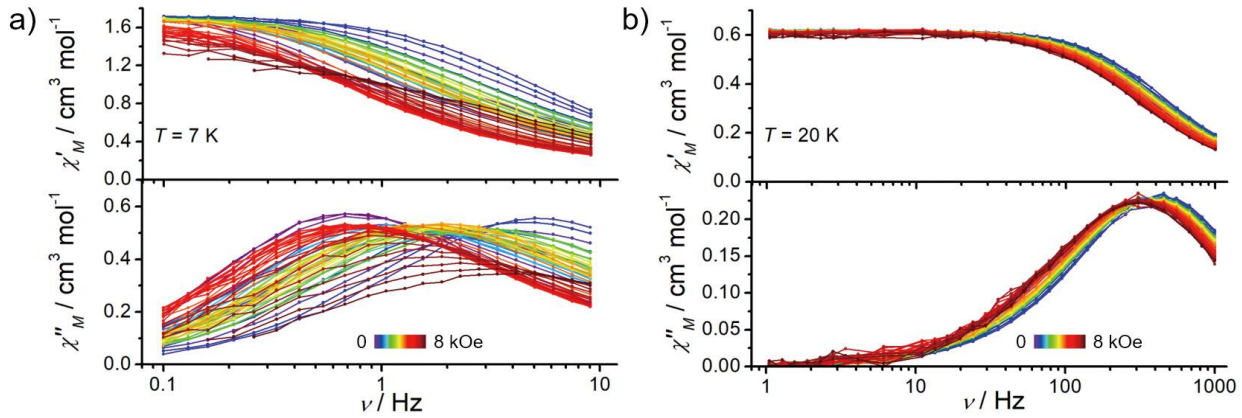

Figure S13. Field dependences of ac magnetic susceptibilities at 7 K (a) and 20 K (b) for **1**. The solid lines are guides for the eyes.

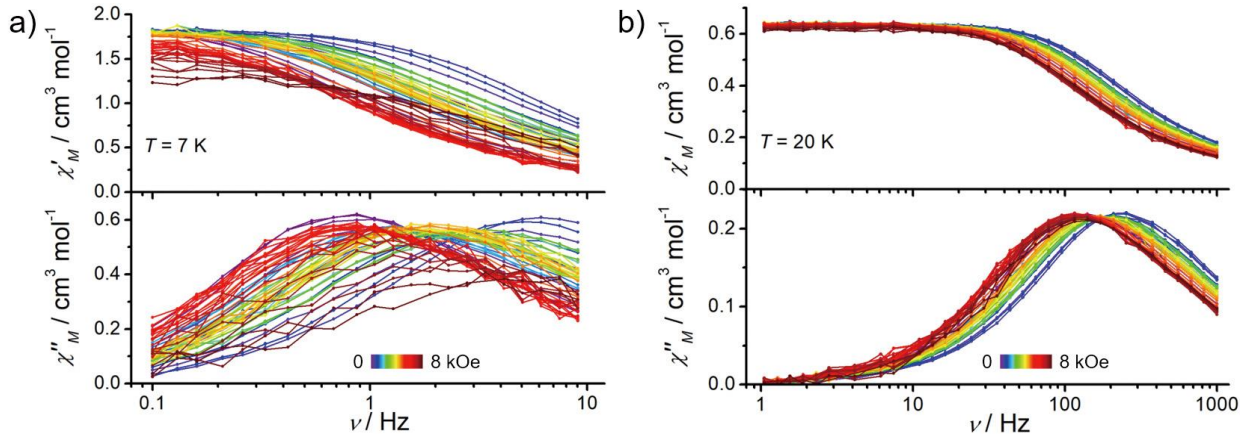

Figure S14. Field dependences of ac magnetic susceptibilities at 7 K (a) and 20 K (b) for **2**. The solid lines are guides for the eyes.

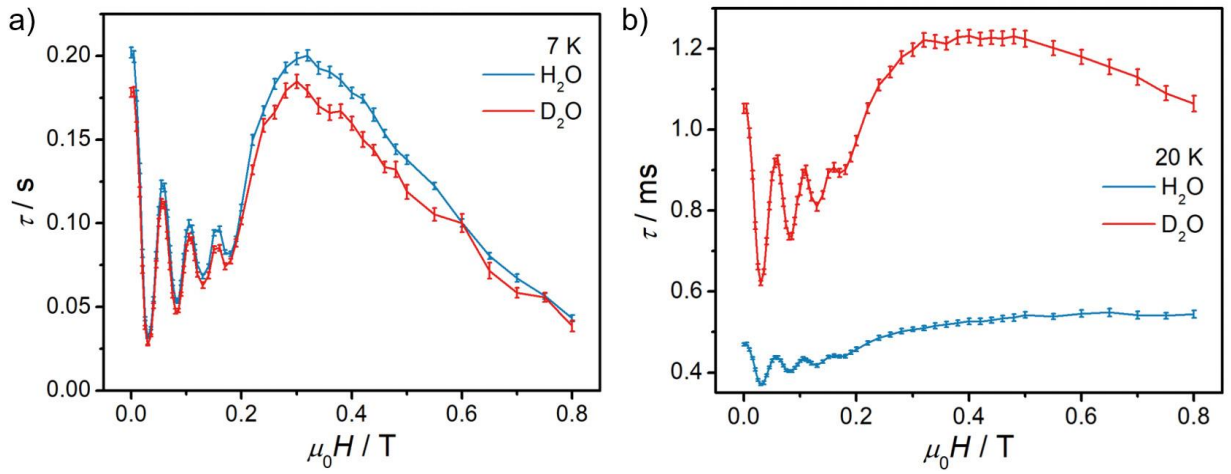

Figure S15. Field dependences of magnetic relaxation times (τ) for **1** (blue) and **2** (red) at 7 K (a) and 20 K (b).

4. *Ab initio* calculations

Ho atom and neighboring waters and other close atoms were described by ANO-RCC-VDZP basis set, while the distant atoms were described by ANO-RCC-VDZ basis sets,[5] accounting for the scalar relativistic effects in the Douglas-Kroll-Hess formulation.[6] The Cholesky decomposition of bi-electronic integrals was employed.[7] The active space of the CASSCF method included ten electrons spanning seven 4*f*-type orbitals of the Ho^{III}. All roots of total spin $S = 2$, $S = 1$ and $S = 0$ were computed, while a subset of them were mixed subsequently by spin-orbit interaction in RASSI.[6,8] The obtained spin-orbit basis was used further by SINGLE_ANISO[9] for the computation of the parameters of the ligand field, *g*-tensors, and magnetism.[10]

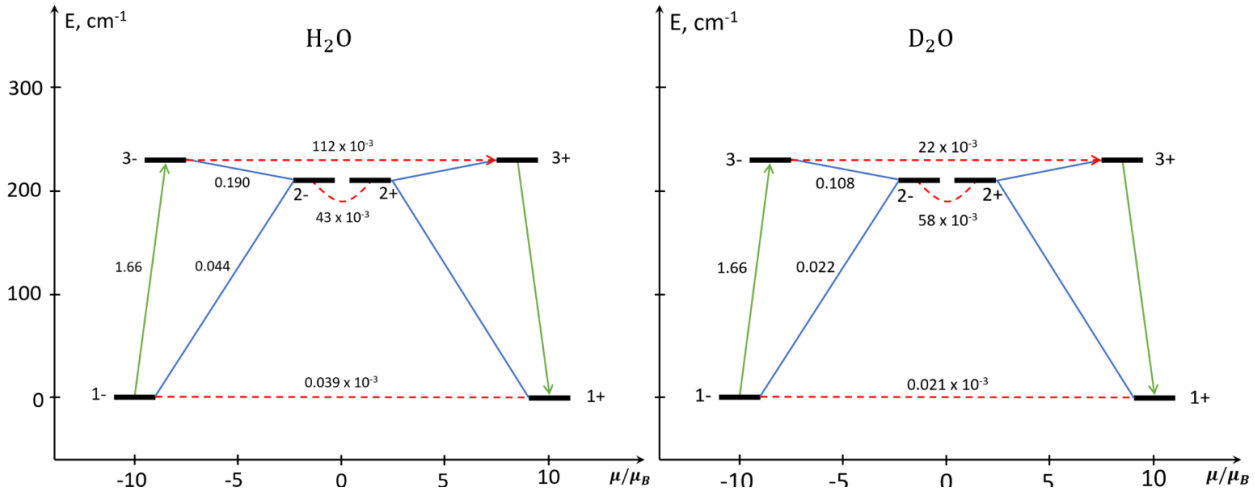

Figure S16. Magnetization blocking diagrams and the dominant relaxation path (path with arrows) in **1** and **2** respectively. Here, the black lines represent the localized states corresponding to three lowest doublets. The other horizontal lines and their associated numbers represent the quantum tunnelling process and their corresponding tunnelling splitting gap. Meanwhile, number on other lines is average transition magnetic moment matrix elements taken from *ab initio* calculations which qualitatively indicates the strength of population transition between localized states.

Table S4. Energies of the low-lying states of the ground multiplet J = 8 of the Ho^{III} ion in the investigated complexes, obtained at CASSCF/RASSI/SINGLE_ANISO level of theory. The g_Z values are given for the low-lying 3 Ising doublet states. Note that $g_X = g_Y = 0$ for an Ising doublet.

1 (H_2O)		**2 (D_2O)**	
Energy (cm^{-1})	***g*z**	**Energy (cm^{-1})**	***g*z**
0.0 $0.0+39.3\times10^{-6}$	19.860	0.0 $0.0+21.0\times10^{-6}$	19.860
212.37 $212.37+43.0\times10^{-3}$	19.716	216.69 $216.69+57.6\times10^{-3}$	19.741
233.27 $233.27+111.9\times10^{-3}$	17.116	236.38 $236.38+22.3\times10^{-3}$	17.167
252.92 253.31 265.88 268.86 274.04 281.29 284.05 298.67 298.68 312.01 312.12 …		256.90 257.21 269.47 273.53 276.97 285.69 286.92 302.50 302.79 315.19 315.20 …	

5. Relaxation energy spectrum

From *ab initio* results and the experimental data, we know that the ligand field in both investigated complexes dominate over the hyperfine coupling between the electronic spin of the metal ion Ho^{III} and its nuclear spin. The latter, in its turn, dominates over the super-hyperfine interaction between the nuclear spins of protium/deuterium and the metal ion's electronic spin. Hence, the effective Hamiltonian for the splitting of an electronic doublet in the electronic localized basis[5,6] can be approximately modelled as:

$$\mathcal{H}_0 \approx \begin{pmatrix} 0 & \Delta/2 \\ \Delta/2 & 0 \end{pmatrix} + A_{hf}\tilde{S}_z I_z + \sum_{i=1,\ldots,10} A_{shf}\tilde{S}_z I_{z,i} + g_z\mu_B\tilde{S}_z H_z\,, \qquad (1)$$

where Δ is the tunnelling splitting gap of the investigating electronic doublet, $\tilde{S}_z$ is the pseudospin 1/2 corresponding to the electronic doublet, A_{hf} and A_{shf} are respectively the hyperfine and super-hyperfine coupling constants, I_z is the nuclear spin operator of Ho^{III} ion along the easy axis of the electronic doublet, and $I_{z,i}$ is the nuclear spin operator of protium/deuterium nuclear spin with *I* = 1/2 (protium) or 1 (deuterium) along the easy axis. The last term in Eq. (1) is responsible for the Zeeman interaction.

As explained in the main text, relaxation of both complexes **1** and **2** depends strongly on the electronic tunnel splitting and the splitting of the electronic doublet under hyperfine and super-hyperfine interactions, especially on the bandwidth of each hyperfine-electronic level under super-hyperfine interaction. This plays an important role in broadening the quantum tunnelling windows. This width can be found by exactly diagonalizing Eq. (1). However, by making use of the order of magnitude of each interaction we can find this broadening width in a simpler way. Indeed, whether the super-hyperfine interaction is ferromagnetic or antiferromagnetic, the entire width will be the energy difference between two states where all protium/deuterium spins are aligned in the same direction, but this direction is either the same or opposite to the one of the metal ion spin. If both have the same contact bonding between the water/heavy water molecules and the centered metal ion Ho^{III}, this leads to a value of $5A_{shf}$ for the width in complex **1** and $10A_{shf}$ in complex **2** as the nuclear spin number of protium is 1/2 and deuterium's one is 1. In other words, the broadening width of each hyperfine-electronic level under the effect of the super-hyperfine interaction in **2** is twice in **1**. The fact that the spin value of deuterium is twice of protium also results in a much denser density of states considering that for 10 nuclear spins of *I* = 1, we have in total of 3^{10} split super-hyperfine hyperfine-electronic states comparing to 2^{10} states if *I* = 1/2. A broader width and a denser density of the super-hyperfine hyperfine-electronic band in the ground multiplet of **2** thus helps compensating for its smaller tunnel splitting, which results in a faster relaxation at low temperature in **2** comparing to **1**.

6. Relaxation profiles and damping oscillation of the relaxation time ratio

In the previous work[13], it has been showing that relaxation in systems with hyperfine coupling should have three relaxation regimes depending on the magnetic field domain between crossings and anti-crossings of hyperfine-electronic energy levels. This property is manifested as an oscillation in the field-dependent relaxation times. Meanwhile, damping of the oscillation is a consequence of the distribution of the relaxation time in polycrystalline sample.

In the current work, we not only observed the same phenomenon in **1** and **2**, but also a new one where their relaxation times ratio also shows a field-dependent oscillation at high temperature, but no oscillation at low temperature. To confirm the suggested mechanism in the main text, the toy model in the previous work[13] (see SI of Ref[13]) is used again. In particular, the field domain between crossing and anti-crossing point is divided into three regions, each relaxation rate Γ_i $(i = 1,2,3)$ will be assigned to each region where $\Gamma_1 < \Gamma_2 < \Gamma_3$. The relaxation rate Γ_3 in third region, which corresponds to the (nearly) full overlap of the super-hyperfine hyperfine-electronic band, is only activated within a small domain of the applied magnetic field characteristic by the parameter ε. In other words, we have a relaxation profile characterized by $(\Gamma_1, \Gamma_2, \Gamma_3)$ of the widths $\left(\frac{1-\varepsilon}{2}, \frac{1-\varepsilon}{2}, \varepsilon\right) H_0$ where H_0 is the field distance between crossing and anti-crossing point (or half of the field period of the oscillation). For complex **1** and **2**, $\Gamma_i^{(1)}$ must be larger than $\Gamma_i^{(2)}$ at high temperature as explained in the main text.

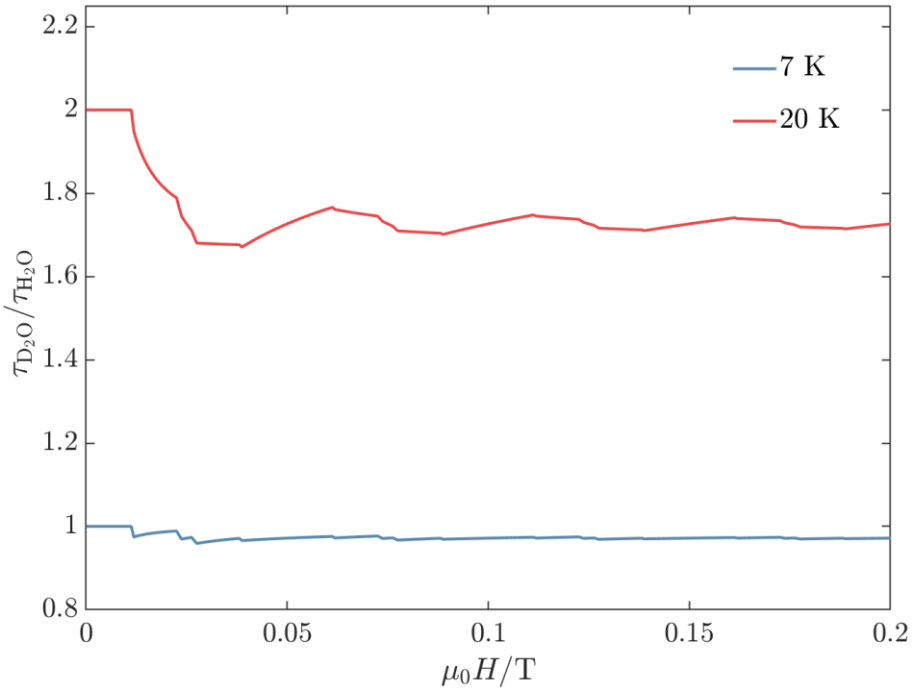

Figure S17. Relaxation times ratio of **1** and **2** as a function of the applied field for polycrystalline sample at 7 K and 20 K. Here the relaxation profiles at 7 K for both complexes are the same $(\Gamma_1, \Gamma_2, \Gamma_3) = (10,15,20)$ except the width ε = 0.05 in **1** and 0.1 in **2**. At 20 K, the same ε = 0.05 in **1** and 0.1 in **2** are used, but $(\Gamma_1, \Gamma_2, \Gamma_3) = (40,50,60)$ in **1** and $(\Gamma_1, \Gamma_2, \Gamma_3) = (20,30,40)$ for **2**. All relaxation rates are chosen arbitrarily for the purpose of illustrating the mechanism and, thus, in arbitrary unit.

As can be seen from Figure S15, when the difference between relaxation profiles of **1** and **2** is large, the observed damping oscillation in the relaxation times ratio is also magnified, despite the fact that both complexes share the same oscillation period. This result is in line with the explanation given in the main text on the change of the relaxation mechanism at high and low temperature as well as clearly shows the isotope effect on the magnetization dynamics in a Holmium-based Single-Molecule magnet.

7. References

[1] G. Sheldrick, *Acta Crystallogr., Sect. A:* **2015**, *71*, 3-8.

[2] O. V. Dolomanov, L. J. Bourhis, R. J. Gildea, J. A. K. Howard, H. Puschmann, *J. Appl. Crystallogr.* **2009**, *42*, 339-341.

[3] G. Sheldrick, *Acta Crystallogr., Sect. C* **2015**, *71*, 3-8.

[4] Y.-C. Chen, J.-L. Liu, W. Wernsdorfer, D. Liu, L. F. Chibotaru, X.-M. Chen, M.-L. Tong, *Angew. Chem. Int. Ed.* **2017**, *56*, 4996-5000.

[5] B. O. Roos, R. Lindh, P.-Å. Malmqvist, V. Veryazov, P.-O. Widmark, *J. Phys. Chem. A* **2005**, *109*, 6575-6579.

[6] B. A. Heß, C. M. Marian, U. Wahlgren, O. Gropen, *Chem. Phys. Lett.* **1996**, *251*, 365-371.

[7] F. Aquilante, P.-Å. Malmqvist, T. B. Pedersen, A. Ghosh, B. O. Roos, *J. Chem. Theory and Comput.* **2008**, *4*, 694-702.

[8] P. Å. Malmqvist, B. O. Roos, B. Schimmelpfennig, *Chem. Phys. Lett.* **2002**, *357*, 230-240.

[9] L. F. Chibotaru, L. Ungur, *J. Chem. Phys.* **2012**, *137*, 064112.

[10] L. Ungur, L. F. Chibotaru, *Chem. – Eur. J.* **2017**, *23*, 3708-3718.

[11] D. Gatteschi, R. Sessoli, J. Villain, *Molecular Nanomagnets*, Oxford University Press, New York, **2006**.

[12] L. T. A. Ho, L. F. Chibotaru, *Phys. Rev. B* **2018**, *97*, 024427.

[13] S.-G. Wu, Z.-Y. Ruan, G.-Z. Huang, J.-Y. Zheng, V. Vieru, G. Taran, J. Wang, Y.-C. Chen, J.-L. Liu, L. T. A. Ho, L. F. Chibotaru, W. Wernsdorfer, X.-M. Chen, M.-L. Tong, *Chem* **2021**, *7*, 982-992.